JACS
JOURNAL OF THE AMERICAN CHEMICAL SOCIETY

Article

pubs.acs.org/JACS

Oligo(ethylene glycol)-Based Thermosensitive Dendrimers and Their Tumor Accumulation and Penetration

Wei Wu,*[,†] Wouter Driessen,[‡] and Xiqun Jiang*[,†]

[†]Department of Polymer Science & Engineering, College of Chemistry & Chemical Engineering, and Jiangsu Provincial Laboratory for Nanotechnology, Nanjing University, Nanjing 210093, People's Republic of China

[‡]iThera Medical GmbH, Neuherberg 85764, Germany

Ⓦ *Web-Enhanced Feature* Ⓢ *Supporting Information*

ABSTRACT: Dendrimers have several featured advantages over other nanomaterials as drug carriers, such as well-defined structure, specific low-nanometer size, and abundant peripheral derivable groups, etc. However, these advantages have not been fully exploited yet to optimize their biological performance, especially tumor penetration, which is a shortcoming of current nanomaterials. Here we show the syntheses of a new class of oligo(ethylene glycol) (OEG)-based thermosensitive dendrimers up to the fourth generation. Each dendrimer shows monodisperse structure. OEG/poly(ethylene glycol) (PEG) moieties with different precise lengths were introduced to the periphery of the fourth-generation dendrimer followed by an antitumor agent, gemcitabine (GEM). The biodistributions of the GEM-conjugated dendrimers were investigated by micro positron emission tomography and multispectral optoacoustic tomography imaging techniques and compared with that of GEM-conjugated poly(amidoamine) (PAMAM). The GEM-conjugated dendrimer with the longest peripheral PEG segments exhibited the most desirable tumor accumulation and penetration and thus had significantly higher antitumor activity than the GEM-conjugated PAMAM.

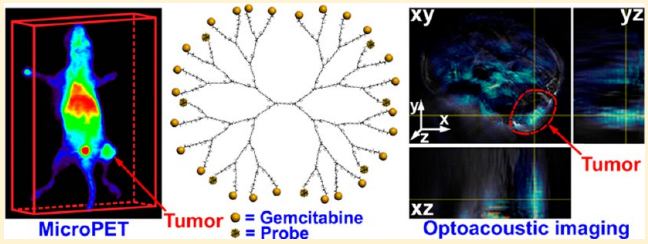

The superiority of nano drug carriers in tumor treatment is essentially based on the enhanced permeability and retention (EPR) effect, which allows them to preferentially accumulate in tumors.[1] However, this superiority is greatly compensated by the poor tumor penetration of current nanocarriers. After extravasation from tumor vessels, nanocarriers are mainly limited to the very adjacent regions due to the high interstitial fluid pressure (IFP), dense interstitial matrix, and abnormal vasculature of tumors, leaving large tumor areas untouched by the carried therapeutic agents and thus greatly limiting their therapeutic effects.[2,3] It has been well demonstrated that the tumor penetration ability of nanomaterials increases with the decrease of their size.[4−7] Accordingly, the low-nanometer size of dendrimers most likely imparts favorable penetration ability. Furthermore, other excellent characteristics of dendrimers, such as monodisperse and highly branched structure, globular shape, presence of internal cavities, and abundant peripheral derivable groups, also make dendrimers very promising in drug delivery.[8−21] The monodisperse and well-defined structure of dendrimers perfectly ensures reproducible pharmacokinetic and pharmacological profiles, which are crucial for a clinical setting to preserve a specific pharmacological activity and prevent unanticipated side effects.[10] The physicochemical properties of dendrimers, such as molecular structure and size, scaffold chemical compositions, and peripheral groups, which greatly influence their interactions with living organisms, can be widely and precisely tuned, allowing regulation of their biological performance designedly.[10−21] The abundant groups on the dendrimer periphery can be utilized to incorporate functional molecules to improve their properties, such as biocompatibility and stimulus-sensitive properties.[20,21] As a typical example in drug delivery, a doxorubicin-loaded bow-tie polyester dendrimer showed the complete eradication of colon carcinoma in mice after a single intravenous injection.[8]

Unfortunately, the intriguing features of dendrimers have not been fully exploited yet to optimize their biological performance, especially tumor penetration. So far, only limited in vitro studies have involved the transport of dendrimers in multicellular tumor spheroids, where targeting ligands are always required to achieve desirable transport ability.[22−25] The tumor penetration of dendrimers has seldom been investigated in vivo up to now. Therefore, it is urgent to develop well-designed dendrimers for drug delivery, which may offer great opportunity to overcome the nanoparticle penetration barrier in tumors and improve significantly the tumor treatment efficacy.

Oligo(ethylene glycol) (OEG)-containing molecules can be used to build dendrimers and provide thermosensitivity and a hydrophilic scaffold, which may potentially benefit the biological applications of the dendrimers.[26−30] So far, several types of OEG-based thermosensitive dendrimers have been synthesized by nucleophilic substitution reactions and con-

Received: November 10, 2013
Published: February 7, 2014

Scheme 1. Synthetic Route of the OEG-Based Dendrimers

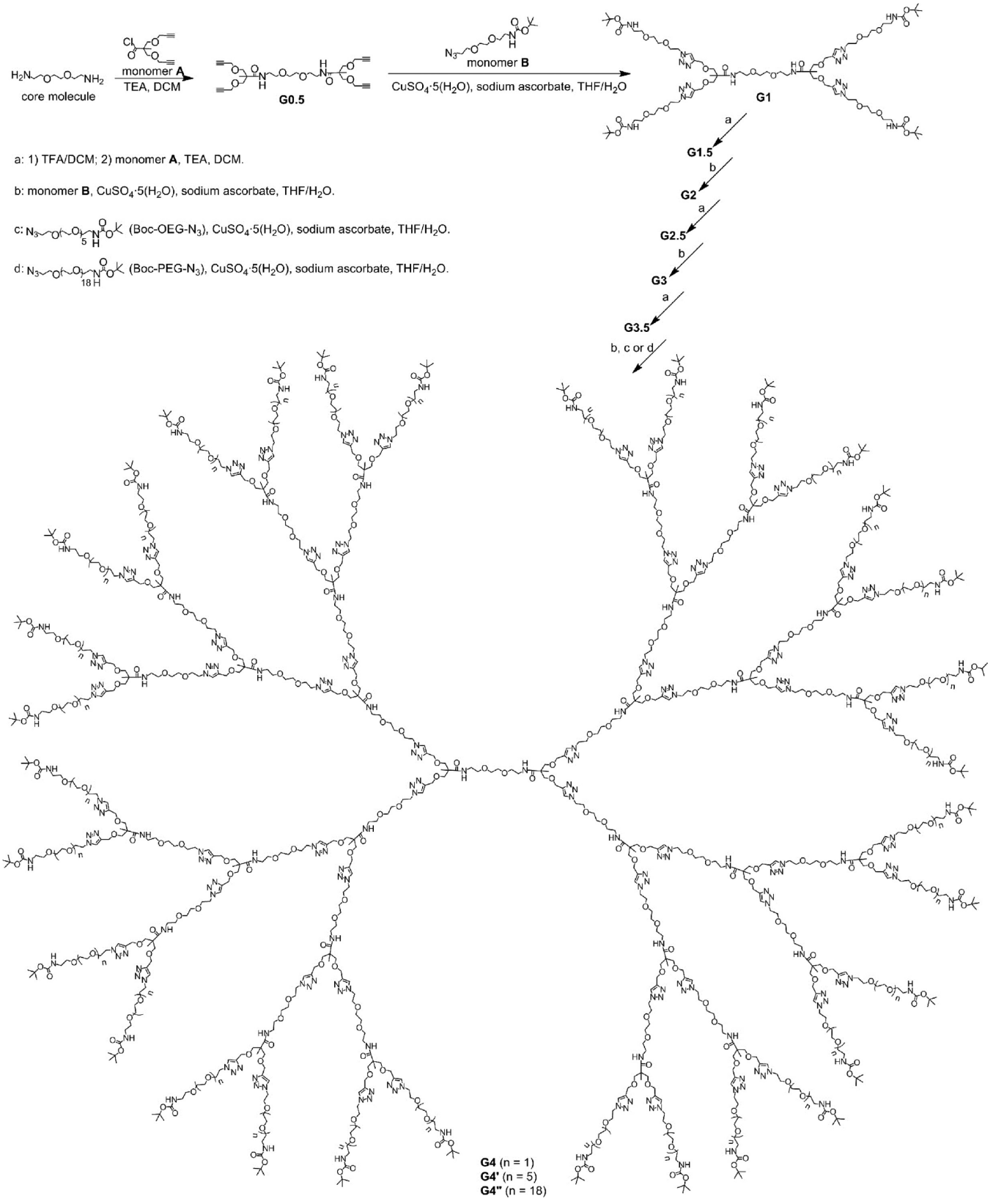

TEA = triethylamine; DCM = dichloromethane; THF = tetrahydrofuran; TFA = trifluoroacetic acid.

vergent growth strategies.[26−29] Nevertheless, these dendrimers have only generation 2 or 3 where the real features of the dendritic architecture may not be apparent. Herein, we focus on the synthesis of a new class of nonionic OEG-based thermosensitive dendrimers and their conjugations with drugs and in vivo behaviors. The dendrimers up to the fourth

dx.doi.org/10.1021/ja411457r | J. Am. Chem. Soc. 2014, 136, 3145−3155

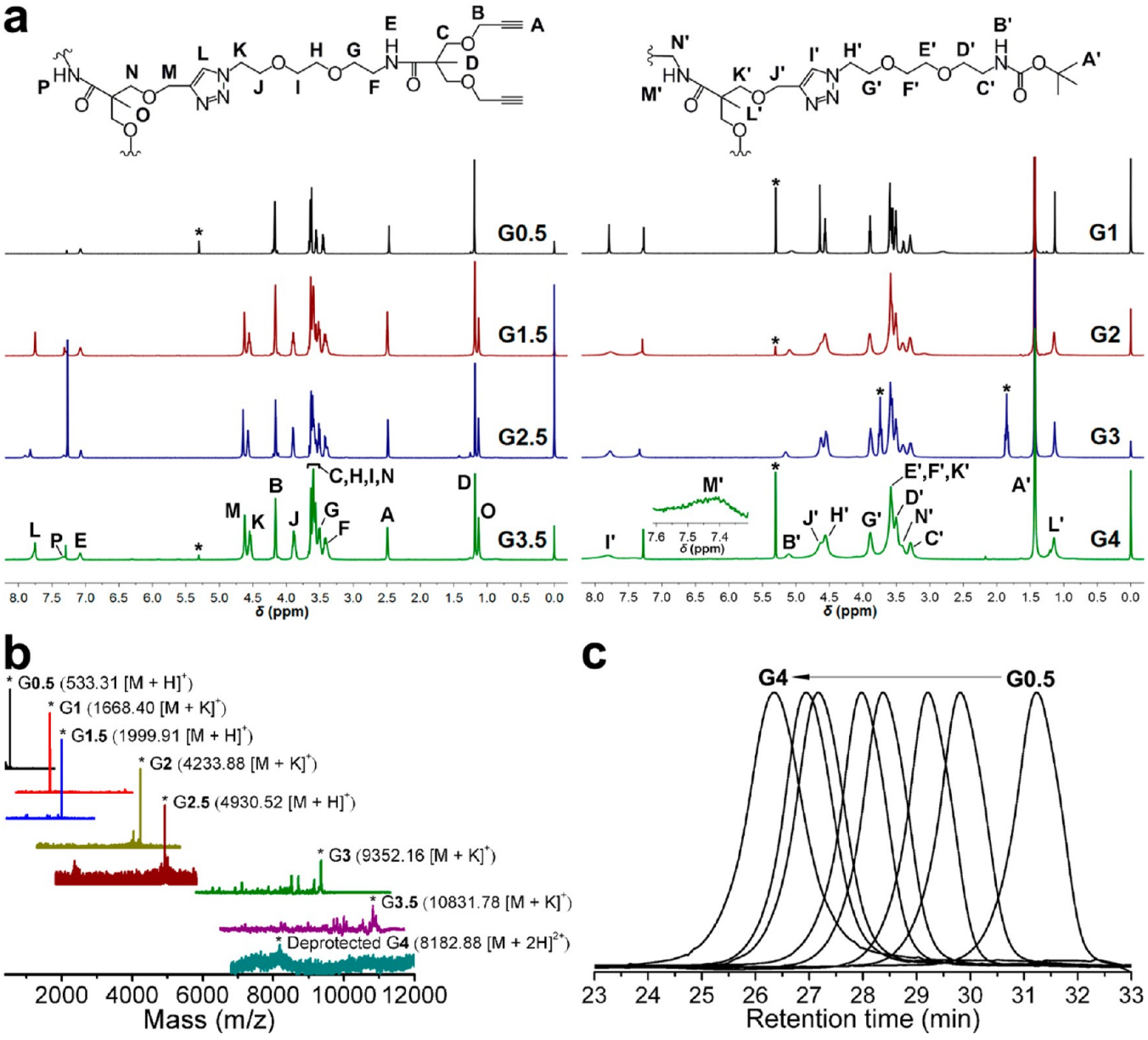

Figure 1. Characterizations of the dendrimers G0.5−G4: (a) ^{1}H NMR spectra (the signals labeled with an asterisk are attributed to residual dichloromethane or tetrahydrofuran); (b) MALDI-TOF MS spectra; (c) SEC curves.

generation were synthesized by using Cu(I)-catalyzed alkyne−azide 1,3-dipolar cycloaddition (CuAAC) and amidation coupling reactions. Both of the reactions have high efficiency and produce biofriendly linkages. OEG/poly(ethylene glycol) (PEG) moieties with different precise lengths were introduced to the fourth-generation dendrimer. Each dendrimer showed monodisperse structure. For drug loading, we conjugated covalently an antitumor agent, gemcitabine (GEM), to the fourth-generation dendrimers. The biodistributions of the GEM-conjugated dendrimers were investigated by micro positron emission tomography (micro-PET) and multispectral optoacoustic tomography (MSOT) imaging techniques and compared with that of GEM-conjugated poly(amidoamine) (PAMAM). The in vivo antitumor activities of the GEM-conjugated dendrimer with the longest peripheral PEG segments versus the GEM-conjugated PAMAM were also evaluated.

RESULTS AND DISCUSSION

To ensure the monodisperse structures, we selected CuAAC and amidation reactions to build dendrimers. Scheme 1 displays the synthetic route of the dendrimers with diaminotris(ethylene glycol) as the core molecule. Monomer A, which acts as a branching unit, reacts with the core molecule to afford generation 0.5 (G0.5) with four alkynyl groups. Further reaction of G0.5 with monomer B via CuAAC affords generation 1 (G1) with four *tert*-butyloxycarbonyl (Boc)-protected amino end groups. After the Boc protective groups are cleaved and the above process is repeated, the dendrimers of successive generations can be synthesized. Yields higher than 90% can be achieved for each step by carefully controlling the reaction conditions (detailed synthetic procedures and characterization data for all involved new compounds can be found in the Supporting Information, Figures S1−S30). The synthesized dendrimers are terminated by either alkynyl groups

dx.doi.org/10.1021/ja411457r | J. Am. Chem. Soc. 2014, 136, 3145−3155

for half generations or Boc-protected amino groups for full generations, which greatly facilitates their functionalizations.

The dendrimers were fully characterized by proton and carbon nuclear magnetic resonance (^{1}H and ^{13}C NMR) and matrix-assisted laser desorption ionization time-of-flight mass spectrometry (MALDI-TOF MS). From the ^{1}H NMR spectra in Figure 1a, the structural evolution from G0.5 to G4 can be observed clearly, for example, the alternating appearance of alkynyl and Boc groups. For each of half generations G1.5, G2.5, and G3.5, the signal of the methyls in the outer layer locates at ∼1.18 ppm, whereas that of the methyls in the interior layers locates at ∼1.13 ppm, and their integral intensity ratio accords well with the calculated value. For the full generations G1, G2, G3, and G4, by comparing the integral intensities of the signals from the Boc groups (1.44 ppm) and the methyls derived from monomer A (1.13 ppm), the complete reactions between monomer B and the dendrimer precursors can be essentially estimated.

MALDI-TOF MS was used to monitor the accurate formation of dendrimers since this technique is capable of detecting the species resulting from either complete or incomplete coupling reaction. As shown in Figure 1b, in the spectrum of each sample from G0.5 to G2.5, a strong signal from the cation adduct (H^+ or K^+ adduct) of the target dendrimer molecule can be observed at the expected molecular weight without detectable incompletely reacted species. For G3, three signals located at lower mass-to-charge ratio (m/z = 8516.683, 8706.905, and 9158.533) besides the strongest signal derived from the target molecule are observed and result from the loss of Boc groups during ionization. For both G3 and G3.5, none of the MS signals derive from the incomplete coupling reaction, revealing the accurate formation of G3 and G3.5. We have tried to examine G4 by MALDI-TOF MS using different matrix and ionizing agents. In all cases, we have failed due to the large molecular weight of G4 that makes ionization very difficult. In view of this, we tested the MALDI-TOF MS of G4 after cleaving the Boc groups. A single signal resulting from doubly charged $[M + 2H]^{2+}$ was detected, confirming the accurate structure of G4. The dendrimers were further examined by size exclusion chromatography (SEC; Figure 1c). An increase of molecular size from G0.5 to G4 can be clearly observed with low polydispersity indexes (PDIs) and high purities.

The OEG moieties of the dendrimers can form a specific hydrogen bond with water by virtue of the high compatibility between their geometrical structures. When the thermal energy of the system exceeds the hydrogen bond energy at elevated temperature, the interaction with water is diminished and thus thermosensitive behavior appears.[31] At a temperature higher than the lower critical solution temperature (LCST) of a dendrimer, its aqueous solution turns turbid. Therefore, to examine the LCSTs of the synthesized dendrimers, turbidity measurements were performed using ultraviolet and visible (UV−vis) spectroscopy. As shown in Figure 2a, the LCSTs for the solutions of G2, G3, and G4 in deionized water at a concentration of 0.25 mg/mL are 31, 24, and 17 °C, respectively. In contrast, for the solution of G1 at the same concentration, the LCST behavior was not observed within 100 °C due to its relatively high hydrophilicity. The LCST of G1 in deionized water at a concentration of 2 mg/mL is measured to be 53 °C (Figure 2a). These results reveal that the LCSTs of the dendrimers decrease with the increase of the dendrimer generation and concentration. Furthermore, the LCSTs of the

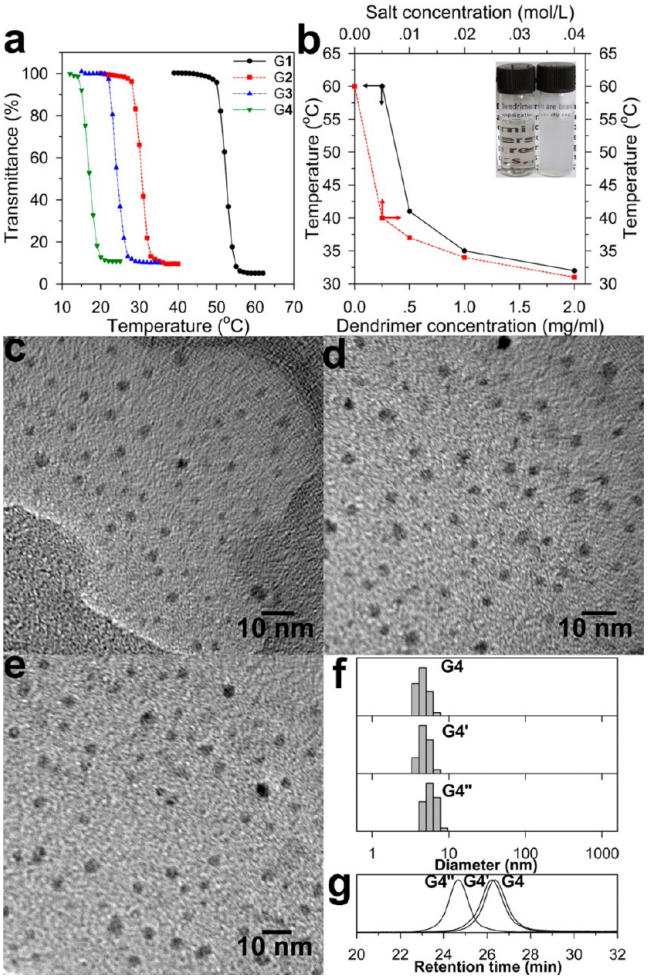

Figure 2. (a) Temperature dependence of light transmittance for the solutions of G1 (2 mg/mL), G2 (0.25 mg/mL), G3 (0.25 mg/mL), and G4 (0.25 mg/mL) in deionized water. (b) LCST dependences of G4′ on its concentration in deionized water (red) and salt concentration in PBS (pH 7.0) (black). The inset shows a photograph of G4′ in deionized water at a concentration of 1.0 mg/mL at 25 °C (left) and 50 °C (right). Typical TEM images of G4 (c), G4′ (d), and G4″ (e). (f) DLS histograms of G4 (top), G4′ (middle), and G4″(bottom). (g) SEC curves of G4, G4′, and G4″.

dendrimers remain invariant between pH 5 and pH 8, which is associated with the low pK_a of the 1,4-substituted 1,2,3-triazole linkage.[32] For all the half generation dendrimers, we did not observe their LCST behaviors because of their low water solubility, showing the influence of end groups.

From the results of the LCST studies, it can be concluded that the water solubility of G4 is lower than 0.25 mg/mL at room temperature. To improve the solubility, Boc-OEG-N_3 and Boc-PEG-N_3 (Scheme 1) were used to replace monomer B in the last synthesis step, and two corresponding dendrimers, G4′ and G4″, were synthesized (detailed synthetic procedures and characterization data for all involved new compounds can be found in the Supporting Information, Figures S31−S46). The monodisperse molecular weights of Boc-OEG-N_3 and Boc-PEG-N_3 (Figures S36 and S44) and the high efficiency of the CuAAC coupling reaction ensure the monodisperse structures of G4′ and G4″, which are characterized by ^{1}H and ^{13}C NMR (Figures S37, S38, S45, and S46). The LCSTs of G4′ in deionized water at concentrations of 0.25, 0.5, 1.0, and 2.0 mg/mL are 60, 41, 35, and 32 °C, respectively (Figure 2b and

dx.doi.org/10.1021/ja411457r | J. Am. Chem. Soc. 2014, 136, 3145−3155

inset); by contrast, G4″ does not display LCST behavior within 100 °C even at concentrations up to 10 mg/mL, indicating the enhanced water solubility of G4′ and G4″ with respect to G4. To evaluate the effect of salt on the thermosensitive behaviors of the dendrimers, we examined the LCSTs of G4′ (0.25 mg/mL) in phosphate buffer solution (PBS) in the presence of different concentrations of NaCl, revealing that the LCST decreases with the increase of salt concentration (Figure 2b).

The morphological structures and sizes of G4, G4′, and G4″ were examined by transmission electron microscopy (TEM) and dynamic light scattering (DLS). TEM images (Figure 2c–e) show that all three types of dendrimers have spherical shapes with narrowly distributed sizes. No significant differences in morphology and size are observed between G4 and G4′, and both of them show a mean diameter of ∼3.5 nm. A slightly larger diameter of G4″ is found to be ∼4.3 nm. The DLS measurements determine the mean diameters of G4, G4′, and G4″ to be 4.6, 4.9, and 5.8 nm in THF solutions, respectively (Figure 2f). The low water solubility of G4 limits its DLS measurement in aqueous medium, while the DLS results of G4′ and G4″ in water are found to be very similar to those in THF. The size variation of the dendrimers was also determined by SEC (Figure 2g), which shows the increase of molecular size in the order G4, G4′, and G4″ as well as their low PDIs and high purities.

The biocompatibilities of G4′ and G4″ were assessed preliminarily by their effect on the apoptosis of 4T1 murine mammary gland tumor cells. Typically, the cells were incubated with G4′ and G4″ for 24 h at 37 °C at doses increasing from 62.5 μg/mL to 1 mg/mL and analyzed by flow cytometry by staining early and late apoptosis and necrosis with annexin V and propidium iodide (Figure 3a and inset). It can be observed that the dendrimers do not induce significant apoptosis and necrosis when compared to the control even at doses up to 1 mg/mL, indicating their low cytotoxicity. G4 was not tested due to its low water solubility at 37 °C.

To evaluate the application potentials of the dendrimers in drug delivery, we conjugated GEM to the fourth-generation dendrimers by synthesizing beforehand a succinate-based GEM ester derivative with Boc protections on 4-NH_2 and 3′-OH (*d*-GEM, Scheme 2; its synthetic procedures and characterization data can be found in the Supporting Information, Figures S47–S49). Scheme 2 shows the synthetic route of the dendrimer–GEM conjugates. On the basis of the ^{1}H NMR analyses (Supporting Information, Figures S50–S55), it can be calculated that about 23–25 GEM molecules are attached to one molecule of the dendrimers on average.

We studied the thermosensitive behaviors of the dendrimer–GEM conjugates. The LCSTs of a 2 mg/mL solution of G4–GEM in 0.15 M PBS at pH 7 and 8 are 62 and 47 °C, respectively. At pH 5 and 6, no LCST behavior was observed within 100 °C, because more amino groups on G4–GEM would be protonized at these acid conditions and thus its water solubility would be enhanced. The 0.15 M PBS was used because of the equal salt concentration of normal saline. For G4′–GEM and G4″–GEM, we could not detect their thermosensitive behaviors at a concentration of 2 mg/mL in 0.15 M PBS at pH 5–8 due to their high water solubility. Although further optimization is required to utilize the thermosensitiveness of the dendrimers in drug delivery, this intrinsic property may significantly expand their potential applications.

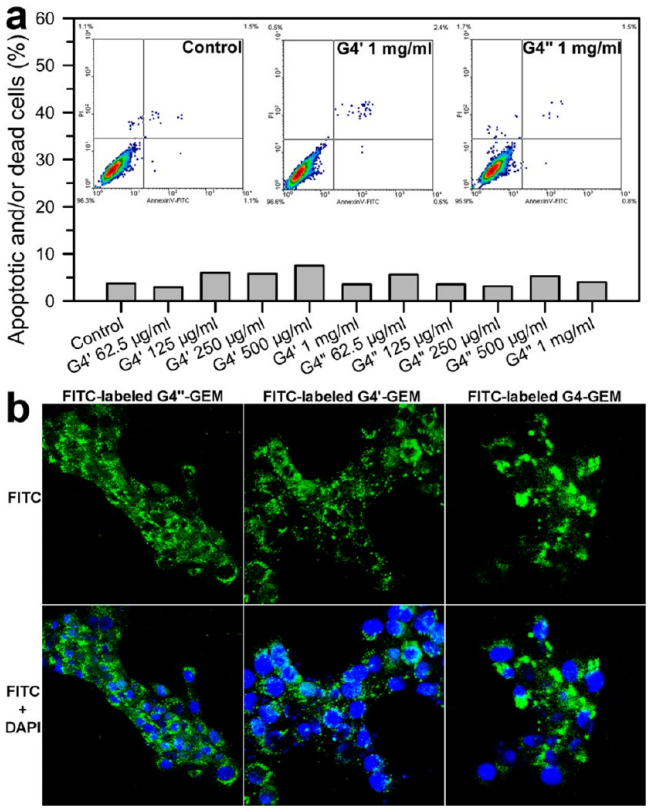

Figure 3. (a) Percentage of early apoptopic, late apoptotic, and/or dead 4T1 murine mammary gland tumor cells after the treatments with G4′ and G4″ at different concentrations for 24 h. After incubation and washings, the cells were stained with annexin V and propidium iodide and analyzed by flow cytometry (inset). (b) CLSM images of 4T1 cells incubated with FITC-labeled dendrimer–GEM conjugates at 37 °C for 4 h. The cell nuclei were stained by 4′,6-diamidino-2-phenylindole (DAPI).

To compare the overall drug delivery behaviors of our dendrimers with those of the commercially available dendrimer PAMAM, we also synthesized GEM-conjugated PAMAM (PAMAM–GEM; Supporting Information, Scheme S1) through the amidation reaction between the amino groups on PAMAM and the carboxylic acid group on *d*-GEM by using the PAMAM with an ethylenediamine initiator core and 32 peripheral amino groups since our fourth-generation dendrimers have the same amount of peripheral groups. On the basis of the ^{1}H NMR analyses (Supporting Information, Figures S56 and S57), it can be calculated that about 20 GEM molecules are attached to one molecule of PAMAM on average. For control experiments, the acetylated PAMAM was also synthesized by the reaction between PAMAM and acetic anhydride. About 28 surface amino groups are acetylated on one molecule of PAMAM on average on the basis of the ^{1}H NMR analyses (Supporting Information, Figure S58).

Confocal laser scanning microscopy (CLSM) was used to trace the cellular uptakes of G4–GEM, G4′–GEM, G4″–GEM, and PAMAM–GEM after they were labeled with fluorescein isothiocyanate (FITC). CLSM images show that all the samples can be easily internalized by 4T1 cells and do not exhibit significant differences in cellular uptake (Figure 3b; Supporting Information, Figure S59). The punctuate fluorescence patterns in the cytoplasm regions together with no significant cellular uptake at 4 °C (data not shown) for the four

dx.doi.org/10.1021/ja411457r | J. Am. Chem. Soc. 2014, 136, 3145–3155

Scheme 2. Synthetic Route of the Dendrimer−GEM Conjugates

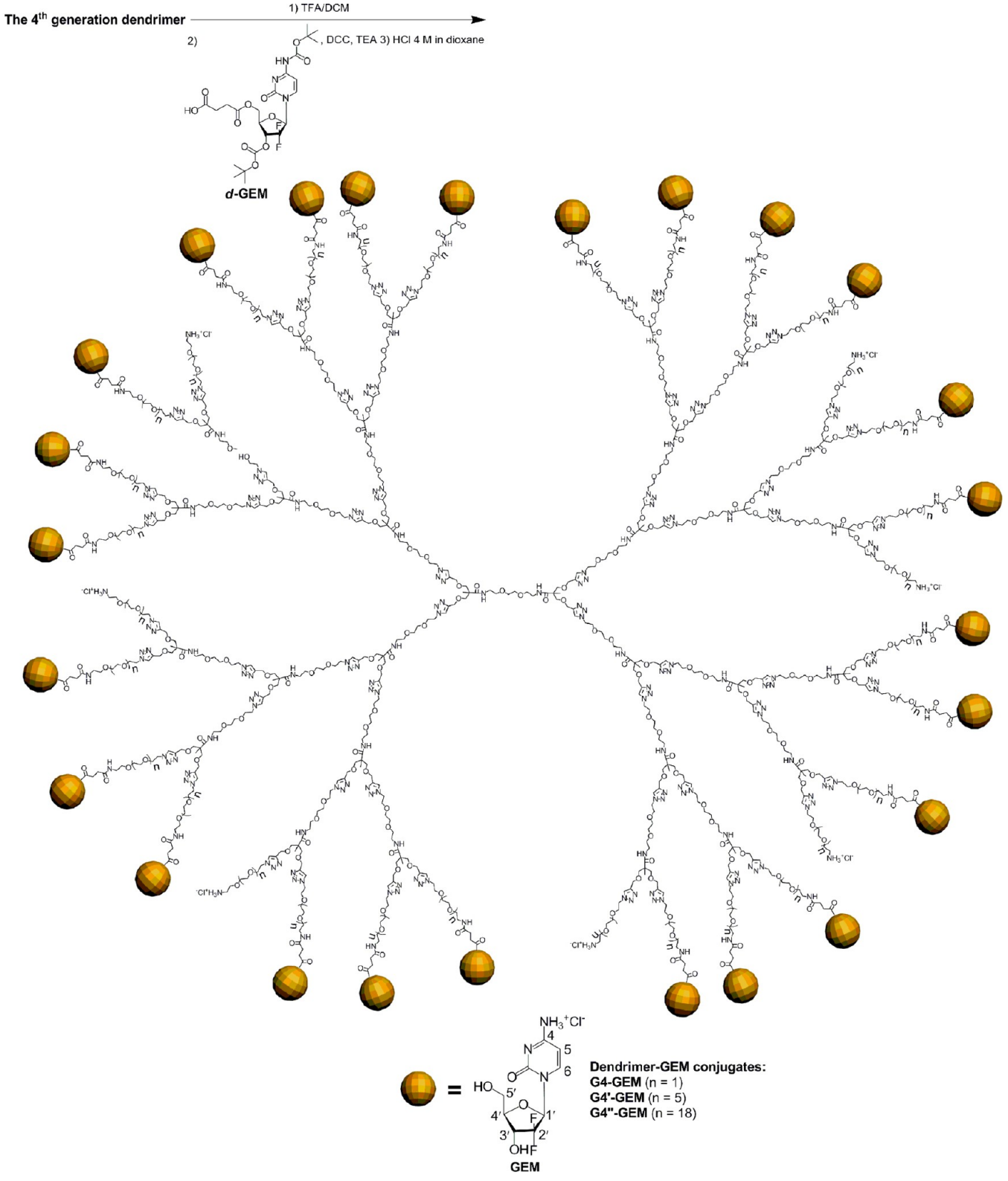

DCC = N, N'-dicyclohexylcarbodiimide.

samples suggest that the conjugates are mainly internalized by the cells through an endocytosis process.

The in vivo behaviors of G4−GEM, G4′−GEM, and G4″−GEM in subcutaneous 4T1 mammary tumor-bearing mice were investigated and compared with that of PAMAM−GEM by using micro-PET after the conjugates were labeled with radioactive nuclide fluorine-18 (^{18}F) through the reaction between the amino groups on the conjugates and *N*-succinimidyl 4-[^{18}F]fluorobenzoate ([^{18}F]SFB). This image-based technique can substantially reduce the number of animals

dx.doi.org/10.1021/ja411457r | *J. Am. Chem. Soc.* 2014, 136, 3145−3155

required and limit the interindividual variability since the same animals can be imaged at multiple time points. The use of a subcutaneous tumor model instead of an orthotopic tumor model is to exclude the interference of the uptakes by surrounding glandular tissues when the tumor uptakes of the molecules are analyzed. Three-dimensional (3D) reconstruction of whole-body images at different time points after injection of the radio-labeled dendrimer−GEM conjugates via the tail vein was conducted (Figure 4 and Web enhanced

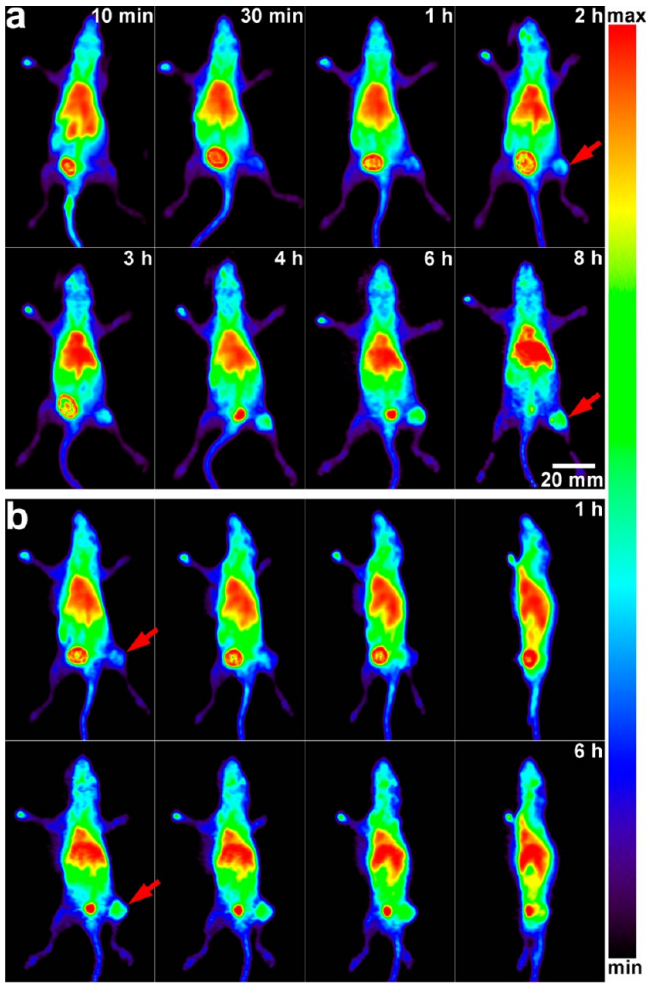

Figure 4. (a) 3D whole-body micro-PET images of a subcutaneous 4T1 tumor-bearing mouse at different time points after tail-vein injection of ^{18}F-labeled G4″--GEM. (b) Rotational views of the 3D whole-body micro-PET images at 1 h (top) and 6 h (bottom) after tail-vein injection of ^{18}F-labeled G4″−GEM. The arrows indicate the tumor region. Movie files depicting the complete 360° rotational views of the 3D whole-body micro-PET images of the subcutaneous 4T1 mammary tumor-bearing mice at different time points after tail-vein injection of ^{18}F-labeled G4″−GEM, G4′−GEM, G4−GEM, and PAMAM−GEM can be found in Web-enhanced objects 1, 2, 3, and 4, respectively.

objects 1, 2, 3, and 4). Also, the quantifications of the radioactivities in different tissues at different times after injection were performed (Supporting Information, Figure S60). For each sample of G4−GEM, G4′−GEM, and G4″−GEM, the kidney shows the highest uptake among all the organs at 10 min postinjection (pi), indicating that they are mainly excreted via the renal route (Figure S60a). The uptake values are calculated to be 30.3%, 75.4%, and 68.1% injected dose per gram of tissue (ID/g) for G4″−GEM, G4′−GEM, and G4−GEM, respectively, indicating that G4′−GEM and G4−GEM are much more susceptible to renal excretion than G4″−GEM. In addition, substantial reductions of the kidney uptakes are observed from 10 to 30 min pi (the uptake values become 11.6%, 27.5%, and 10.8% ID/g for G4″−GEM, G4′−GEM, and G4−GEM, respectively, at 30 min pi), and then the uptakes vary slowly. In the heart, G4″−GEM shows a slow concentration decrease over the whole study period (22.9% ID/g at 10 min and 10.7% ID/g at 8 h pi), whereas, from 10 to 30 min pi, the heart uptake drops rapidly from 19.4% to 5.1% ID/g for G4′−GEM and from 8.6% to 1.5% ID/g for G4−GEM and then changes slowly for both the samples (Figure S60b). The blood clearances of G4″−GEM, G4′−GEM, and G4−GEM were evaluated by monitoring radioactivity from the cardiac pool over time. The concentration−time profiles (Figure S60c) for the three samples fit well into two-compartment models. The elimination half-lives of G4″−GEM, G4′−GEM, and G4−GEM are calculated to be 753, 146, and 85 min, respectively. The liver uptakes at 10 min pi are about 13.5%, 15.3%, and 8.6% ID/g for G4″−GEM, G4′−GEM, and G4−GEM, respectively. These values decrease to 10.6%, 5.5%, and 1.6% ID/g at 30 min pi, respectively, and then exhibit slow variations. Notably, the tumor uptake of G4″−GEM increases continuously from 10 min to 8 h pi and reaches ∼8.7% ID/g at 8 h pi; by contrast, for G4′−GEM and G4−GEM, the maxima of tumor uptake among all the test time points are found to be ∼2.0% ID/g at 4 h pi and ∼1.8% ID/g at 10 min pi, respectively, revealing the much better tumor targeting ability of G4″−GEM. Apparently, the significant biodistribution differences of the three samples are caused by the different lengths of the OEG/PEG on the periphery since no other structural difference exists. The lengthened PEG segments prolong the blood circulation time and significantly increase the tumor accumulation of the dendrimer. Also, they slow the clearance of the dendrimer from the organs, such as the kidney, liver, and heart, as discussed above. On the other hand, for the biodistribution of PAMAM−GEM (Web enhanced object 4 and Figure S60), the kidney uptake maintains a high level over the whole study period (47.3% ID/g at 10 min and 69.2% ID/g at 6 h pi), which is consistent with the published results[33] but different from the cases of G4″−GEM, G4′−GEM, and G4−GEM, whose kidney uptakes decrease rapidly from 10 min pi. The heart uptake of PAMAM−GEM is 6.1% ID/g at 10 min and decreases to 1.1% ID/g at 30 min and then changes slowly. Its blood clearance profile, which is evaluated by monitoring radioactivity from the cardiac pool over time, also fits well into the two-compartment model, and the elimination half-life is calculated to be 52 min. The liver uptake of PAMAM−GEM (18.4% ID/g at 10 min and 19.9% ID/g at 6 h pi) is significantly higher than those of G4″−GEM, G4′−GEM, and G4−GEM within the 6 h monitoring duration. Compared to G4″−GEM, G4′−GEM, and G4−GEM, the tumor uptake of PAMAM−GEM is lower, and the maximum of its tumor uptake among all the test time points is found to be ∼0.68% ID/g at 1 h pi. The different biodistribution pattern of PAMAM−GEM with respect to G4″−GEM, G4′−GEM, and G4−GEM may be associated with its scaffold structure, which is different from those of the other three dendrimers.

We next focus on the intratumoral behaviors of the dendrimer−GEM conjugates. Interestingly, from the 3D whole-body images and movie (Figure 4 and Web enhanced

dx.doi.org/10.1021/ja411457r | J. Am. Chem. Soc. 2014, 136, 3145−3155

object 1) as well as tomographic slices (Figure 5; Supporting Information, Figure S61) for the case of G4″−GEM, it can be

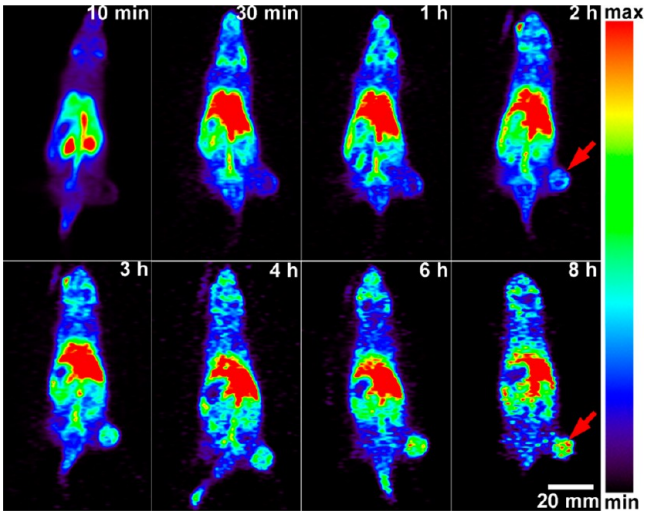

Figure 5. Coronal micro-PET slices (0.78 mm thick) through the tumor center of a 4T1 tumor-bearing mouse at different time points after tail-vein injection of ^{18}F-labeled G4″−GEM. The arrows indicate the tumor region.

clearly seen that its intratumoral distribution is initially heterogeneous. In some regions of the tumor, its concentrations are initially low and then gradually increase as time goes by. These regions should be poorly vascularized, and the injected molecules cannot directly reach there via blood-borne delivery. In this case, diffusion driven by concentration difference becomes the primary mode for molecule transport to these poorly perfused regions. Eventually, G4″−GEM permeates through the entire tumor in a desirable concentration, demonstrating its extraordinary tumor penetration ability. Although the tumor penetration abilities of G4′−GEM and G4−GEM are not as good as that of G4″−GEM, they can also reach the tumor center as time elapses (Web enhanced objects 2 and 3 and Supporting Information, Figures S62 and S63). We believe that the reduction in permeability of G4′−GEM and G4−GEM is associated with their lower tumor uptakes, which reduce the concentration difference between the regions near the tumor vasculature and the poorly vascularized regions, which serves as the driving force of diffusion, when compared to that in the case of G4″−GEM. By contrast, the concentration of PAMAM−GEM in the tumor center remains at a very low level over the whole monitoring duration (Web enhanced object 4 and Supporting Information, Figure S64), revealing its lower tumor penetration ability compared to those of G4″−GEM, G4′−GEM, and G4−GEM. Apart from the low tumor uptake, its different scaffold structure compared to those of G4″−GEM, G4′−GEM, and G4−GEM may be a factor causing the different permeability.

We further studied the tumor accumulation and penetration of G4″−GEM by MSOT imaging after labeling the conjugate with a near-infrared dye (NIR-797) since G4″−GEM exhibits the best overall in vivo properties among the four types of dendrimer−GEM conjugates. The MSOT technique can monitor probes over a longer period than micro-PET (^{18}F has a short half-life of 110 min) and separate different photoabsorbing molecules on the basis of their spectroscopic absorption differences. The orthotopic 4T1 tumor model is used because MSOT has a significant ability to distinguish the tumor from surrounding tissues,[34,35] and the performance of G4″−GEM in both orthotopic and subcutaneous tumor models can be compared. The spatial distributions of G4″−GEM and oxyhemoglobin (HbO_2) in orthotopic 4T1 tumor-bearing mice were reconstructed by MSOT at different times after injection of the NIR-797-labeled G4″−GEM via the tail vein (Figure 6a). It is found that the HbO_2 signals that reflect the locations of blood vessels are abundant in the outer layer but rare in the center of the tumor. The distributions of the HbO_2 and G4″−GEM signals are different, indicating the extravasation of G4″−GEM from blood vessels and further penetration into the tumor matrix. The quantifications of the G4″−GEM signal intensity per unit tumor area and signal distribution area in tumors at different time points pi (Figure 6b) show that the tumor uptake of G4″−GEM at 24 h pi is highest among the test time points, whereas its distribution area increases continuously from 6 to 48 h pi, confirming the gradual diffusion of G4″−GEM in tumors. To better understand the tumor penetration of G4″−GEM, the signals of the labeled G4″−GEM and hemoglobin were colocalized at 24 h pi and the oxygen saturation in blood (SO_2) was estimated by comparing the MSOT signal strength of HbO_2 and deoxyhemoglobin (Hb; Figure 6c). The regions with lower SO_2 are observed in the center of the tumor and represent the hypoxic areas. It is noteworthy that the signals of G4″−GEM are strong not only in the high SO_2 regions but also in the low SO_2 regions where viable vasculature required for probe delivery is probably lacking, indicating the good tumor penetration ability of G4″−GEM.[36] In a previous work, the intratumoral distributions of indocyanine green within 24 h pi, an $\alpha_v\beta_3$-targeting fluorescent agent (IntegriSense 750) within 6 h pi, and gold nanorods (with dimensions of 10 × 38 nm) within 24 h pi in 4T1 tumors with sizes similar to those in our case have been investigated by using MSOT.[36] Most of these probes are found in or close to blood vessels in tumors, and few probes can be observed in the hypoxic regions of tumors within the monitoring durations. By comparison to these probes, the much better tumor penetration ability of G4″−GEM is clearly evidenced. Additionally, it has been well documented that nanocarriers can generally penetrate only a few tens of micrometers deep or less into the tumor matrix.[4,37] The reason for the good tumor penetration ability of G4″−GEM is not thoroughly understood at present. The high tumor accumulation and low-nanometer size of the dendrimer should be contributory factors.

Finally, we investigated the antitumor activities of G4″−GEM versus PAMAM−GEM in vitro and in vivo. The in vitro cytotoxicities of G4″−GEM, PAMAM−GEM, and acetylated PAMAM against 4T1 murine mammary gland tumor cells were determined with a positive control of GEM hydrochloride. As shown in Figure S65 (Supporting Information), both G4″−GEM and PAMAM−GEM exhibit cytotoxicity levels similar to that of GEM hydrochloride at equal GEM concentrations. The acetylated PAMAM does not show significant cytotoxicity at concentrations up to 1 mg/mL, which is comparable to the case of G4″. The in vivo antitumor performance of G4″−GEM and PAMAM−GEM was assessed by using subcutaneous 4T1 mammary tumor-bearing mice as model animals and compared with that of GEM hydrochloride at a dosage normalized to be 20 mg of GEM equivalent per kilogram of body weight. The groups treated with G4″, acetylated PAMAM, and saline were used as controls (the molar amounts of G4″ and acetylated PAMAM were equal to those of G4″−GEM and PAMAM−

dx.doi.org/10.1021/ja411457r | J. Am. Chem. Soc. 2014, 136, 3145−3155

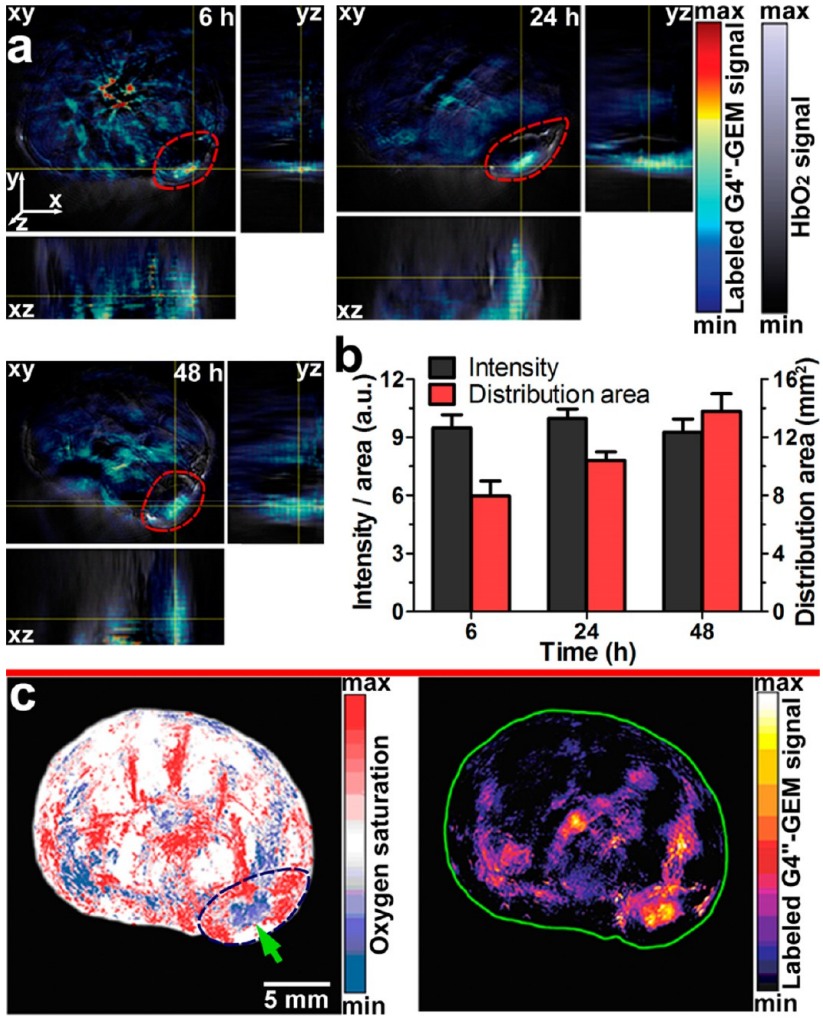

Figure 6. (a) Orthogonal views of the MSOT images of an orthotopic 4T1 tumor-bearing mouse at different time points after tail-vein injection of NIR-797-labeled G4″−GEM showing overlaid HbO_2 and NIR-797-labeled G4″−GEM signals. The 3D coordinate system defines the orientations and positions of the orthogonal views, and the dashed circles indicate the tumor regions. (b) Quantifications of the MSOT signal intensity of the NIR-797-labeled G4″−GEM per unit tumor area and its intratumoral distribution area that is acquired as a pixel area with a signal value >0 within the tumor region of interest (ROI) at different time points after tail-vein injection of the NIR-797-labeled G4″−GEM. (c) MSOT images showing SO_2 (left) and NIR-797-labeled G4″−GEM (right) signals acquired 24 h after tail-vein injection of NIR-797-labeled G4″−GEM. The two images show exactly the same region. The dashed circle indicates the tumor region, and the arrow indicates the hypoxic zone of the tumor.

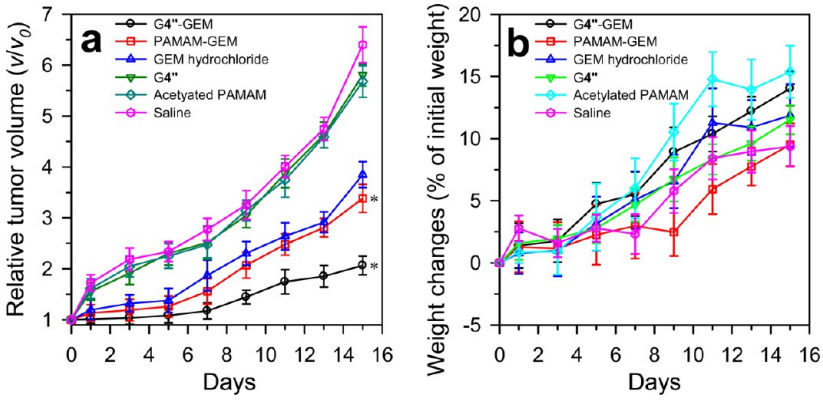

Figure 7. (a) In vivo antitumor effect obtained from each treated group, expressed as the average values of the relative tumor volume, v/v_0 (where v denotes the tumor volume at the test time points and v_0 denotes the corresponding initial tumor volume at the beginning of the treatment). An asterisk indicates $P < 0.05$ (G4″−GEM versus PAMAM−GEM from day 7). (b) Evolution of the body weight of each group during the experiments, expressed as the percentage weight change of the mice relative to the initial body weight. Data are presented as the mean ± SD (n = 8).

dx.doi.org/10.1021/ja411457r | J. Am. Chem. Soc. 2014, 136, 3145−3155

GEM, respectively). Each of the compounds was injected as a solution in 0.2 mL of saline. Fifteen day follow-up experiments were carried out after the administrations. From the tumor volume measurements performed every other day (Figure 7a), it can be observed that G4″−GEM inhibits tumor growth much more efficiently than PAMAM−GEM and GEM hydrochloride. The tumor growth inhibition (TGI) calculated for the group treated with G4″−GEM is 67.7% on the 15th day (see the Supporting Information for the calculation method). By contrast, the TGIs obtained from the groups treated with PAMAM−GEM and GEM hydrochloride are 47.2% and 39.8%, respectively, and much lower than that of the group treated with G4″−GEM. Apparently, the enhanced antitumor activity of G4″−GEM relative to PAMAM−GEM should be contributed mainly by its high tumor accumulation and deep tumor penetration. Both G4″ and acetylated PAMAM do not exhibit an observable inhibition effect. Over the course of the study, the weights (Figure 7b) and clinical situations of all the tested groups were scrutinized and did not appear to be influenced by the treatments of the three formulations of GEM when compared to those of the saline-treated group, indicating the well-tolerated dose level of drug and the negligible toxicity of G4″ and acetylated PAMAM imposed on the experimental mice.

In conclusion, we synthesized a new class of dendrimers with generation-dependent thermosensitivity. The high efficiency of the CuAAC and amidation coupling reactions imparts the dendrimers monodisperse structures that would greatly favor their reproducible pharmacokinetic and pharmacological profiles. An antitumor agent, GEM, was conjugated to the fourth-generation dendrimers, and the drug-conjugated dendrimers also exhibit thermosensitivity, though further LCST optimization is required to match these properties with the tumor microenvironment. By using micro-PET and MSOT imaging techniques, we demonstrated that our GEM-conjugated dendrimers had significant superiority over GEM-conjugated PAMAM in tumor accumulation and penetration. Lengthening the PEG segments on the periphery of the dendrimers can significantly improve the dendrimers' circulation time and tumor-targeting ability. Accordingly, our GEM-conjugated dendrimer with the longest peripheral PEG segments exhibited significantly higher antitumor activity compared to the GEM-conjugated PAMAM.

■ ASSOCIATED CONTENT

Ⓢ Supporting Information

Experimental details, characterization data for all new compounds, and additional results. This material is available free of charge via the Internet at http://pubs.acs.org.

Ⓦ Web-Enhanced Features

Web enhanced objects 1−4 showing the complete 360° rotational views of the 3D whole-body micro-PET images of the subcutaneous 4T1 mammary tumor-bearing mice at different time points after tail-vein injection of ^{18}F-labeled G4″−GEM, G4′−GEM, G4−GEM, and PAMAM−GEM, respectively, in AVI format are available in the HTML version of the paper.

■ AUTHOR INFORMATION

Corresponding Authors

wuwei@nju.edu.cn
jiangx@nju.edu.cn

Notes

The authors declare no competing financial interest.

■ ACKNOWLEDGMENTS

This work was supported by the National Natural Science Foundation of China (Grant Nos. 51033002 and 51273090) and Program for Changjiang Scholars and Innovative Research Team in University. We thank Yan Wang and Chenglong Yan at Wuxi Molecular Imaging CRO Co., Ltd. for the micro-PET measurements.

■ REFERENCES

(1) Taurin, S.; Nehoff, H.; Greish, K. *J. Controlled Release* **2012**, *164*, 265−275.
(2) Jain, R. K. *Annu. Rev. Biomed. Eng.* **1999**, *1*, 241−263.
(3) Jain, R. K.; Stylianopoulos, T. *Nat. Rev. Clin. Oncol.* **2010**, *7*, 653−664.
(4) Perrault, S. D.; Walkey, C.; Jennings, T.; Fischer, H. C.; Chan, W. C. W. *Nano Lett.* **2009**, *9*, 1909−1915.
(5) Cabral, H.; Matsumoto, Y.; Mizuno, K.; Chen, Q.; Murakami, M.; Kimura, M.; Terada, Y.; Kano, M. R.; Miyazono, K.; Uesaka, M.; Nishiyama, N.; Kataoka, K. *Nat. Nanotechnol.* **2011**, *6*, 815−823.
(6) Tang, L.; Fan, T. M.; Borst, L. B.; Cheng, J. J. *ACS Nano* **2012**, *6*, 3954−3966.
(7) Yu, S. L.; Zhang, Y. J.; Wang, X.; Zhen, X.; Zhang, Z. H.; Wu, W.; Jiang, X. Q. *Angew. Chem., Int. Ed.* **2013**, *52*, 7272−7277.
(8) Lee, C. C.; Gillies, E. R.; Fox, M. E.; Guillaudeu, S. J.; Fréchet, J. M. J.; Dy, E. E.; Szoka, F. C. *Proc. Natl. Acad. Sci. U.S.A.* **2006**, *103*, 16649−16654.
(9) Kannan, S.; Dai, H.; Navath, R. S.; Balakrishnan, B.; Jyoti, A.; Janisse, J.; Romero, R.; Kannan, R. M. *Sci. Transl. Med.* **2012**, *4*, 130ra46.
(10) Kaminskas, L. M.; Boyd, B. J.; Porter, C. J. *Nanomedicine* **2011**, *6*, 1063−1084.
(11) Mintzer, M. A.; Ginstaff, M. W. *Chem. Soc. Rev.* **2011**, *40*, 173−190.
(12) Lee, C. C.; MacKay, J. A.; Fréchet, J. M. J.; Szoka, F. C. *Nat. Biotechnol.* **2005**, *23*, 1517−1526.
(13) Meijer, E. W.; van Genderen, M. H. P. *Nature* **2003**, *426*, 128−129.
(14) Lim, J.; Simanek, E. E. *Adv. Drug Delivery Rev.* **2012**, *64*, 826−835.
(15) Lim, J.; kostiainen, M.; Maly, J.; da Costa, V. C. P.; Annunziata, O.; Pavan, G. M.; Simanek, E. E. *J. Am. Chem. Soc.* **2013**, *135*, 4660−4663.
(16) Ihre, H.; De Jesús, O. L. P.; Fréchet, J. M. J. *J. Am. Chem. Soc.* **2001**, *123*, 5908−5917.
(17) Parrott, M. C.; Benhabbour, S. R.; Saab, C.; Lemon, J. A.; Parker, S.; Valliant, J. F.; Adronov, A. *J. Am. Chem. Soc.* **2009**, *131*, 2906−2916.
(18) Lamanna, G.; Russier, J.; Dumortier, H.; Bianco, A. *Biomaterials* **2012**, *33*, 5610−5617.
(19) Shen, Y. Q.; Ma, X. P.; Zhang, B.; Zhou, Z. X.; Sun, Q. H.; Jin, E. L.; Sui, M. H.; Tang, J. B.; Wang, J. Q.; Fan, M. H. *Chem.—Eur. J.* **2011**, *17*, 5319−5326.
(20) Jain, K.; Kesharwani, P.; Gupta, U.; Jain, N. K. *Int. J. Pharm.* **2010**, *394*, 122−142.
(21) Ramireddy, R. R.; Raghupathi, K. R.; Torres, D. A.; Thayumanavan, S. *New J. Chem.* **2012**, *36*, 340−349.
(22) Sunoqrot, S.; Liu, Y.; Kim, D.-H.; Hong, S. *Mol. Pharmaceutics* **2013**, *10*, 2157−2166.
(23) Waite, C. L.; Roth, C. M. *Bioconjugate Chem.* **2009**, *20*, 1908−1916.
(24) Dhanikula, R. S.; Argaw, A.; Bouchard, J.-F.; Hildgen, P. *Mol. Pharmaceutics* **2008**, *5*, 105−116.
(25) Al-Jamal, K. T.; Al-Jamal, W. T.; Wang, J. T.-W.; Rubio, N.; Buddle, J.; Gathercole, D.; Zloh, M.; Kostarelos, K. *ACS Nano* **2013**, *7*, 1905−1917.

(26) Aathimanikandan, S. V.; Savariar, E. N.; Thayumanavan, S. *J. Am. Chem. Soc.* **2005**, *127*, 14922−14929.
(27) Li, W.; Zhang, A. F.; Chen, Y.; Feldman, K.; Wu, H.; Schlüter, A. D. *Chem. Commun.* **2008**, 5948−5950.
(28) Li, W.; Wu, D. L.; Schlüter, A. D.; Zhang, A. F. *J. Polym. Sci., Part A: Polym. Chem.* **2009**, *47*, 6630−6640.
(29) Abdel-Rahman, M. A.; Al-Abd, A. M. *Eur. J. Med. Chem.* **2013**, *69*, 848−854.
(30) Hayder, M.; Fruchon, S.; Fournié, J.-J.; Poupot, M.; Poupot, R. *Sci. World J.* **2011**, *11*, 1367−1382.
(31) Kjellander, R.; Florin, E. *J. Chem. Soc., Faraday Trans. 1* **1981**, *77*, 2053−2077.
(32) Katritzky, A. R.; Pozharskii, A. F. *Handbook of Heterocyclic Chemistry*, 2nd ed.; Elsevier Science Ltd.: Oxford, U.K., 2000; pp 377−379.
(33) Sadekar, S.; Ray, A.; Janàt-Amsbury, M.; Peterson, C. M.; Ghandehari, H. *Biomacromolecules* **2011**, *12*, 88−96.
(34) Wang, X. D.; Pang, Y. J.; Ku, G.; Xie, X. Y.; Stoica, G.; Wang, L. H. V. *Nat. Biotechnol.* **2003**, *21*, 803−806.
(35) Mallidi, S.; Luke, G. P.; Emelianov, S. *Trends Biotechnol.* **2011**, *29*, 213−221.
(36) Herzog, E.; Taruttis, A.; Beziere, N.; Lutich, A. A.; Razansky, D.; Ntziachristos, V. *Radiology* **2012**, *263*, 461−468.
(37) Zhen, X.; Wang, X.; Xie, C.; Wu, W.; Jiang, X. Q. *Biomaterials* **2013**, *34*, 1372−1382.